Chemical Science

ROYAL SOCIETY OF CHEMISTRY

EDGE ARTICLE

View Article Online
View Journal | View Issue

Cite this: *Chem. Sci.*, 2026, **17**, 8795

All publication charges for this article have been paid for by the Royal Society of Chemistry

Directing structural transformation in gold(I)–carborane nanoclusters to unlock ultrafast hypergolic ignition

Hao-Hui Xie,[a] Wen-Jing Yang,[b] Ze-Jian Li,[a] Ying-Zheng Ren,[a] Nian Si,[a] Peng-Fei Liu,[a] Yong-Xing Tang, *[a] Wen-Chao Zhang *[ac] and Peng-Fei Cui *[acd]

The construction of structurally transformable nanoclusters and the elucidation of their transformation mechanisms remain challenging. Furthermore, uncovering how structural changes govern their properties is even more elusive. Herein, a novel "cation-dissociation & anion-reassembly" structural transformation strategy is investigated. Specifically, $[Au_{18}S_8(m\text{-P}\hat{}\text{P})_6][Cl]_2$ (**Au_{18}**) can transform into $[Au_8S_4(m\text{-P}\hat{}\text{P})_2]$ (**Au_8**) through the synergistic effects of cations and anions: cations act as Lewis acids to dissociate **Au_{18}**, while anions direct the reassembly of fragments into **Au_8**. Moreover, a novel bis-tetrahedral cluster $[Au_7(m\text{-P}\hat{}\text{P})_2(o\text{-}^{nido}\text{P}\hat{}\text{P})_2]$ ($o\text{-}^{nido}$P^P = 7,8-bis(diphenylphosphine)-*nido*-carborane, **Au_7**) was synthesized by a ligand exchange strategy with **Au_{18}**. Concerning high energy densities of carborane backbones, a droplet test was conducted, and the results showed that both **Au_{18}** and **Au_8** were not able to be ignited by white fuming nitric acid, whereas **Au_7** exhibited a very fast ignition delay time of 16(2) ms with high energy densities (heat of combustion, 25.3 kJ g^{-1}). Theoretical calculations reveal that the bis-tetrahedral metal kernel in **Au_7** modifies the electronic structure, lowering the activation barrier for oxidation and thereby shortening the ignition delay time. This work not only provides fundamental insights into the structural transformation pathways of nanoclusters, but also establishes relationships between structures and hypergolic properties, which are meaningful for the design of nanoclusters with tunable properties.

Received 6th February 2026
Accepted 6th March 2026

DOI: 10.1039/d6sc01070a

rsc.li/chemical-science

Introduction

Core–shell architectures, observed across a range of scales from galactic megastructures to atomic dimensions, represent a universal structural motif in natural systems, integrating symmetry with functional topology.[1–5] Studying and understanding their formation, spatial arrangement and transformation mechanisms provides critical insights into the fundamental principles governing natural systems.[4–12] At the molecular level, nanoclusters with metal–ligand core–shell architectures serve as an ideal model system for exploring and understanding such structural patterns, attracting considerable interest in the scope of nanocluster chemistry.[1,13–21] Advances in characterization techniques, particularly single-crystal X-ray diffraction and mass spectrometry, have enabled precise determination of nanocluster structures. However, real-time monitoring of reaction intermediates and elucidating their transformation pathways remain challenging, not to mention tracing the associated structure–property relationships.[22–24] Therefore, elucidating complicated structural transformation processes is essential not only for advanced fundamental understanding of core–shell architectures but also for guiding the rational design of transformable systems with targeted functionalities.[25–28]

Gold(I)–chalcogenide clusters represent one of the popular systems in the gold family owing to their synthetically accessible pathways and remarkable structural integrity,[29–31] and have emerged as one of the ideal candidates for the investigation of transformable nanoclusters. In particular, the controlled modulation of Au(I)–Au(I) aurophilic interactions in gold(I)–chalcogenide clusters—mediated by solvent environments and physical stimuli—enables precise regulation of the pyramidal $[Au_3(\mu_3\text{-S})]^+$ unit assembly into diverse polynuclear architectures.[32–34] Furthermore, the geometries of gold(I)–chalcogenide clusters also exhibit high sensitivity to functional bisphosphine ligands with planar skeletons.[32,35–37] However, the potential for three-dimensional bulky units to serve as backbones remains less explored.[38–40] Bulky units such as adamantane, cryptand and carborane may fail to provide complete

[a]*School of Chemistry and Chemical Engineering, Nanjing University of Science and Technology, 210094 Nanjing, China. E-mail: yongxing@njust.edu.cn; wenchaozhang@njust.edu.cn; pfcui@njust.edu.cn*

[b]*College of Material Engineering, Fujian Agriculture and Forestry University, Fuzhou 350108, China*

[c]*State Key Laboratory of Transient Chemical Effects and Control of China, Shaanxi Applied Physics and Chemistry Research Institute, Xi'an, 710061, China*

[d]*The Key Laboratory of Functional Molecular Solids, Ministry of Education, Wuhu, 241002, China*

kernel protection,[15,41–44] potentially leaving coordination sites exposed and susceptible to rearrangement or decomposition, which may possibly lead to the construction of novel structures of polynuclear gold(I)–chalcogenide clusters.

Following the above analysis, *m*-P^P (1,7-bis(diphenylphosphine)carborane, Scheme S1) with a bulky carborane unit was selected to explore potential structural transformation in gold(I)–chalcogenide families. Two gold(I)–chalcogenide clusters $[Au_{18}S_8(m\text{-P^P})_6][Cl]_2$ (**Au_{18}**) and $[Au_8S_4(m\text{-P^P})_2]$ (**Au_8**) were synthesized by reacting gold precursor $[Au_2Cl_2(m\text{-P^P})]$ with different sulfur sources. **Au_{18}** can transform into **Au_8** and **Au_7** ($[Au_7(m\text{-P^P})_2(o\text{-}^{nido}\text{P^P})_2]$, $o\text{-}^{nido}$P^P = 7,8-bis(diphenylphosphine)-*nido*-carborane) induced by "cation-dissociation & anion-reassembly" and a ligand-exchange strategy, respectively. Furthermore, the droplet test indicated that both **Au_{18}** and **Au_8** were not able to be ignited, while **Au_7** has potential to serve as a hypergolic material with very fast ignition delay time (16 ms). This work elucidates distinct structural transformation pathways, thereby establishing a fundamental framework for understanding and tailoring functional core–shell architectures.

Results and discussion

To assess the potential influence of sulfur sources on the synthesis of gold–chalcogenide clusters, the gold precursor $[Au_2Cl_2(m\text{-P^P})]$ was reacted with H_2S, Na_2S and $S(SiMe_3)_2$ (Scheme 1), and the reactions were monitored by ^{31}P NMR spectroscopy (Fig. S32–S34 and S36), respectively. In each case, three consistent signals were observed in $CDCl_3$ at ~50.0, 48.5, and 20.5 ppm, which can be identified as **Au_{18}**, **Au_8** and the *m*-P^P ligand (Fig. S19), respectively, further confirmed by single crystal X-ray diffraction. The relative intensity of the **Au_8** signal (~48.5 ppm) increased rapidly when the sulfur source was varied in the order $H_2S \rightarrow Na_2S \rightarrow S(SiMe_3)_2$, accompanied by a corresponding decrease in the **Au_{18}** signal at ~50.0 ppm. We attribute this variation in product distribution to the ionic radius of the sulfur sources.

Crystallographic data analyses and electrospray ionization time-of-flight mass spectrometry (ESI-TOF MS) measurement of **Au_{18}** and **Au_8** were performed to elucidate their atomically precise structures. Single crystal analysis indicates that **Au_{18}** crystallizes in the triclinic space group $P\bar{1}$, and the asymmetric unit contains half of the $[Au_{18}S_8(m\text{-P^P})_6]^{2+}$ cation ($Z' = 0.5$) suggesting a C_i symmetry configuration in the crystalline state (Fig. S6). Steric hindrance from the bulky carborane ligands leads to a non-compact, dispersed spatial arrangement of the $[(\mu_3\text{-S})Au_3]^+$ units. As illustrated in Fig. 1a–d, two $[(\mu_3\text{-S})Au_3]^+$ units are linked *via* aurophilic interactions to form a central $[(\mu_3\text{-S})_2Au_6]^{2+}$ dimer (Fig. 1a). This dimeric core is surrounded by six additional $[(\mu_3\text{-S})Au_3]^+$ units that share six gold vertices, thereby exposing 12 coordination sites on the cluster periphery (Fig. 1b). The shell of **Au_{18}** is further occupied by six bisphosphine *m*-P^P ligands (Fig. 1c). In contrast, the single peak observed in the ^{31}P NMR spectrum recorded in diluted solution ($CDCl_3$, CD_3OD and CD_3CN, ~0.02 mg μL^{-1}) suggests a higher S_6 symmetry (Fig. S15 and S29). Furthermore, **Au_{18}** exhibits concentration-dependent behaviors: at a higher concentration (~0.08 mg μL^{-1}), the spectrum of **Au_{18}** splits into three signals ($\delta = 51.71$, 50.79, and 50.22 ppm, Fig. S28), which is presumably attributed to symmetry breaking in the condensed phase. The multiply charged ion peaks at $m/z = 3437.9360$ are unambiguously assigned to the doubly charged ions ($[Au_{18}S_8(m\text{-P^P})_6]^{2+}$, simulated $m/z = 3437.9387$, Fig. S42). The chemical formula is assigned as $[Au_{18}S_8(m\text{-P^P})_6][Cl]_2$, as no other counter anions were present in this system. Unexpectedly, a single crystal of **Au_{18}** with two independent halves of the $[Au_{18}S_8(m\text{-P^P})_6]^{2+}$ cations ($Z' = 2 \times 0.5$) was also collected (Fig. S9–S11, see the SI for details). It shows different packing modes owing to subtle differences in intermolecular interactions (Fig. S6–S12).

The single crystal structure of **Au_8** crystallizes in the $P2_1/c$ space group with A–B–A–B packing modes in the *bc* plane (Fig. S13 and S14). As shown in Fig. 1d–f, its kernel is constructed by four $[(\mu_3\text{-S})Au_3]^+$ units that share four gold atoms to further form a distorted Au_4 square. The remaining four Au atoms adopt a bridging coordination mode, linked by two bidentate *m*-P^P ligands. This neutral structure was further confirmed by the ESI-TOF MS ion peak at $m/z = 2730.2019$ ($[C_{52}H_{62}Au_8B_{20}P_4S_4]^+$), which corresponds well with the simulated peak at $m/z = 2730.2010$ (Fig. S43). Similarly, **Au_8** also displays concentration-

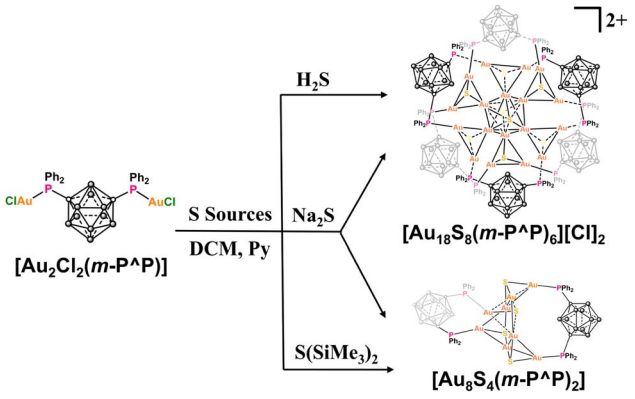

Scheme 1 Reaction of gold precursor $[Au_2Cl_2(m\text{-P^P})]$ with different sulfur sources.

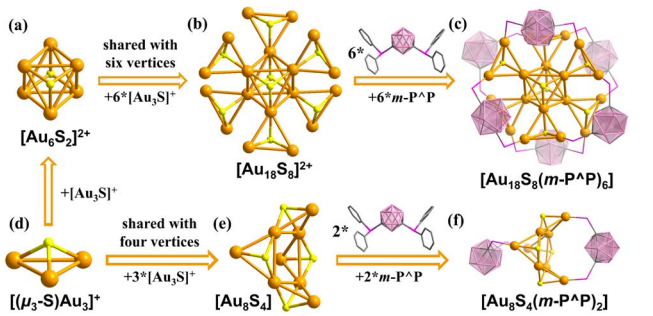

Fig. 1 (a) Inside $[(\mu_3\text{-S})_2Au_6]^+$ structural motifs in **Au_{18}**; (b) inside $[(\mu_3\text{-S})_2Au_6]^+$ structural motifs shared with six $[(\mu_3\text{-S})Au_3]^+$ units to construct **Au_{18}** kernel $[Au_{18}S_8]^{2+}$; (c) single crystal structure of **Au_{18}**. Ph rings are omitted for clarity; (d) $[(\mu_3\text{-S})Au_3]^+$ unit; (e) metal kernel of **Au_8**; (f) single crystal structure of **Au_8**.

dependent behavior in solution. Its dilute solution (0.02 mg μL^{-1} in $CDCl_3$) shows a single peak at $\delta = 48.03$ ppm, indicating a higher symmetry structure (Fig. S31). At a higher concentration (0.06 mg μL^{-1}), the spectrum resolves into two distinct peaks at $\delta = 48.14$ and 48.01 ppm.

It is well known that ions from inorganic salts can either combine directly with cluster surfaces or modulate weak intermolecular interactions between frameworks, thereby inducing structural reconfiguration of the cluster architecture.[34,45,46] To investigate potential binding effects of anions in **Au_{18}**, NH_4BF_4 was selected to react with **Au_{18}** followed by monitoring the reaction pathways (Fig. 2a). Unexpectedly, a new ^{31}P NMR peak emerged at $\delta = 48.7$ ppm within 10 minutes, with its intensity increasing over one hour. This chemical shift signal is consistent with **Au_8**, as further confirmed by single-crystal XRD. Addition of NH_4PF_6 contributes to analogous structural transformation (Fig. S1).

Well-designed experiments are conducted to elucidate the potential mechanism of this unexpected transformation routes. First, the individual cation (NH_4^+) or anion (BF_4^-/PF_6^-) is introduced into the **Au_{18}** system to identify which active species operate in this process. However, no new ^{31}P NMR signals are detected upon addition of the corresponding salts NH_4Cl, $NaBF_4$ and $NaPF_6$ (Fig. 2b), respectively, which suggests that

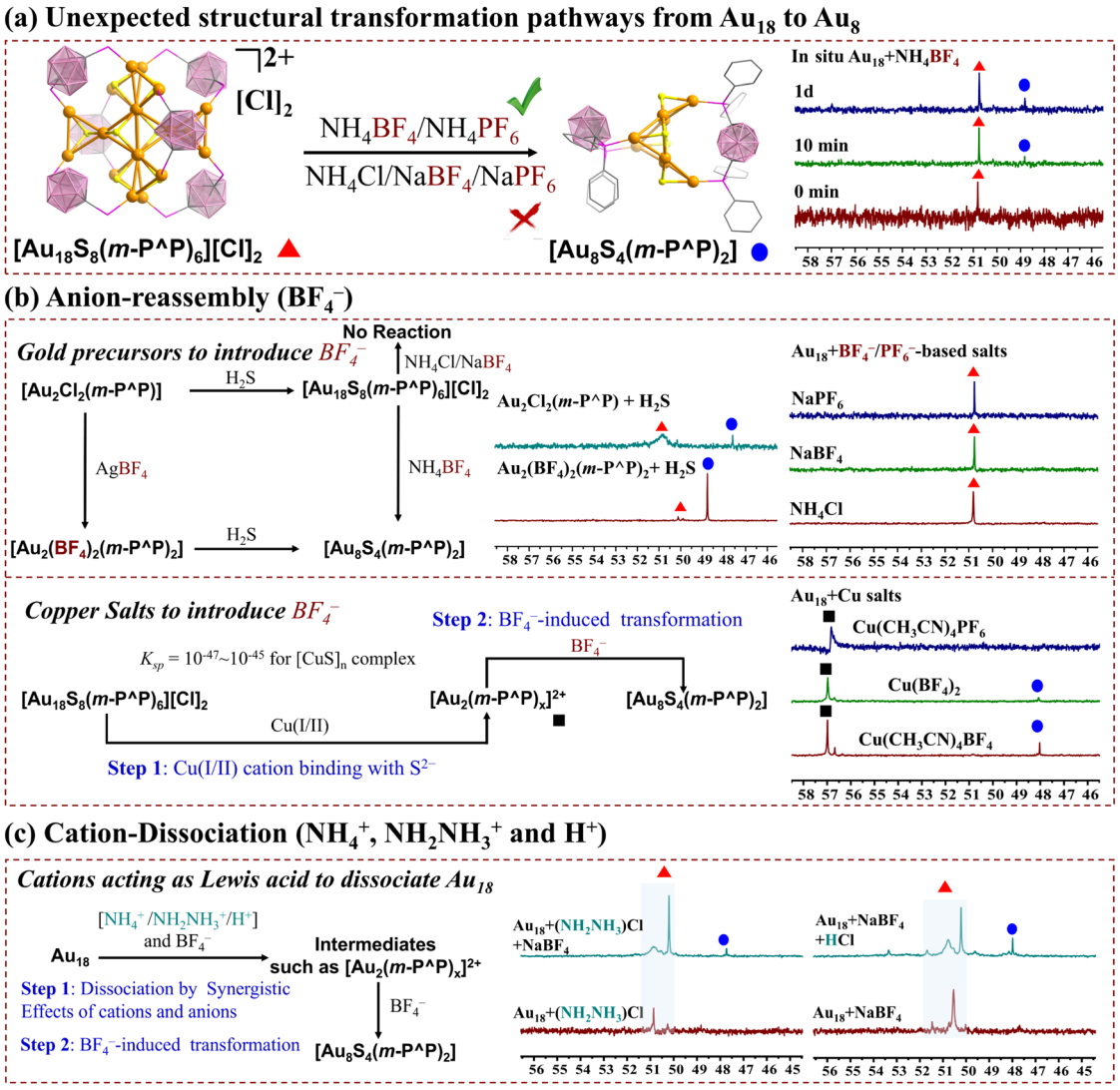

Fig. 2 (a) Schematic illustration of the structural transformation from Au_{18} to Au_8, and *in situ* ^{31}P NMR spectra of Au_{18} reacting with NH_4BF_4. Addition of NH_4BF_4 (3 mg in 0.1 mL MeOH) to a solution of Au_{18} (5 mg in 0.2 mL $CDCl_3$) resulted in a large amount of white precipitate. The low conversion may be attributed to a poorly dissolved reaction system. (b) Left: Schematic illustration of H_2S reacting with different gold precursors; middle: the crude ^{31}P NMR spectra of different gold precursors reacting with H_2S; right: ^{31}P NMR spectra of Au_{18} reacting with NH_4Cl, $NaBF_4$ and $NaPF_6$, respectively. Reaction conditions: $CDCl_3$ = 0.3 mL; MeOH = 0.1 mL; Au_{18} = 5 mg; salts = 3 mg; 2 days; below: schematic mechanism of anions and the ^{31}P NMR spectrum of Au_{18} reacting with Cu salts. Reaction conditions: $CDCl_3$ = 0.3 mL; Au_{18} = 5 mg, salts = 3 mg; 2 days; (c) Schematic mechanism of cations and substitution by $NH_3NH_2^+$ and H^+. The red spectra: Au_{18} (10 mg) + salts (5 mg) in dichloromethane (DCM) and CH_3OH reacted for 1 day, then the replacement of solution with $CDCl_3$ (0.2 mL). The green spectra: intermediately adding $NaBF_4$ (3 mg) in MeOH (0.15 mL) and HCl (~0.5 μL) into the above red spectra systems, respectively.

this transformation may involve the synergistic effects of cations and anions.

Then, the potential effects of BF_4^- were studied to examine the influence of anions. As shown in Fig. 2b, $[Au_2Cl_2(m\text{-P^P})]$ was reacted with $AgBF_4$ to yield a new gold precursor $[Au_2(m\text{-P^P})_2][BF_4]_2$, whose composition was confirmed by ESI-TOF MS (observed $m/z = 709.7504$ for $[Au_2C_{52}H_{60}B_{20}P_4]^{2+}$ and calculated $m/z = 709.7504$, Fig. S41). The ^{31}P NMR spectrum displayed a major peak at 57.02 ppm along with a minor signal at 57.50 ppm (Fig. S26). Single-crystal X-ray diffraction identified this minor species as the neutral byproduct $[Au_2(m\text{-}^{nido}P\text{^}P)_2]$ ($m\text{-}^{nido}P\text{^}P$ represents the diboration of *m*-P^P, Fig. S5). Bubbling H_2S into this system, the single crystal of $\mathbf{Au_8}$ was again obtained. A comparative analysis of the $\mathbf{Au_{18}}$: $\mathbf{Au_8}$ product ratios synthesized from $[Au_2Cl_2(m\text{-P^P})]$ (~5.5 : 1, Fig. S32) and $[Au_2(m\text{-P^P})_2][BF_4]_2$ (~1 : 10.5, Fig. S35) revealed that the presence of BF_4^- anions may promote the formation of $\mathbf{Au_8}$. Compared to the $\mathbf{Au_8}$ single crystal obtained *via* the $\mathbf{Au_{18}}$ + NH_4BF_4 route, the Au–Au bond distances are nearly identical (Fig. S3), implying the decisive role of BF_4^- ions in directing the formation of the $\mathbf{Au_8}$ structure. To further confirm this, as shown in Fig. 2b, Cu salts $Cu(CH_3CN)_4BF_4$, $Cu(BF_4)_2$ and $Cu(CH_3CN)_4PF_6$ were selected to mix with $\mathbf{Au_{18}}$ for the strong binding affinity of Cu(I/II) towards S atoms (pK_{sp} = 47–45 for copper sulfide complexes). ^{31}P NMR spectra revealed the near disappearance of $\mathbf{Au_{18}}$ signals, accompanied by intense resonances corresponding to $[Au_2(m\text{-P^P})_x]^{2+}$ ($x = 1$ or 2), and weak signals at ~48.0 ppm attributable to $\mathbf{Au_8}$. The oxidation state of copper exerted negligible influence on the reaction. Thus, the whole transformation routes of Cu salts can be simplified into two crucial steps (Fig. 2b): (1) the first step is the dissociation of $\mathbf{Au_{18}}$ into $[Au_2(m\text{-P^P})_x]^{2+}$ driven by the strong binding affinity of Cu(I/II) and S^{2-} atoms; (2) subsequently, $[Au_2(m\text{-P^P})_x]^{2+}$ transferred to $\mathbf{Au_8}$ facilitated by BF_4^-/PF_6^- ions with a small amount of free sulfur sources.

Based on the transformation pathway of Cu salts, we propose that NH_4^+ ions, acting as a Lewis acid analogous to Cu(I/II) cations, cooperate synergistically with BF_4^- anions to facilitate the dissociation of $\mathbf{Au_{18}}$. For NH_4BF_4-induced structural transformation, the signal of $[Au_2(m\text{-P^P})_x]^{2+}$ can be clearly detected with increased concentration of $\mathbf{Au_{18}}$ (Fig. S37). To verify the potential effects of anions, the replacement of NH_4^+ with $NH_2NH_3^+$ to serve as a Lewis acid, followed by the introduction of extra BF_4^- anions, similarly induced the transformation of $\mathbf{Au_{18}}$ into $\mathbf{Au_8}$ (Fig. 2c). Moreover, a small amount of HCl was added into the $\mathbf{Au_{18}}$ + $NaBF_4$ system, which also exhibited the characteristic ^{31}P NMR signal of $\mathbf{Au_8}$ (Fig. 2c). The distinct "cation-dissociation & anion-reassembly" mechanism elucidated here represents an uncommon structural transformation route in nanocluster chemistry, diverging from conventional ligand- or solvent-driven structural transformation pathways.

The distinct open "suspension bridge" architecture combined with the bulk ligand protection shell establishes $\mathbf{Au_{18}}$ as an ideal model for investigating more structural transformation possibilities in metal nanoclusters. Therefore, extra bisphosphine ligands 1,8-(diphenylphosphino)naphthalene (Nap-P^P) and 1,2-bis(diphenylphosphine)carborane (*o*-P^P) with similar P···P distances (~3.2 Å) were selected to react with $\mathbf{Au_{18}}$.

As shown in Fig. 3a, the reaction of $\mathbf{Au_{18}}$ with Nap-P^P ligands led to the decomposition of $\mathbf{Au_{18}}$ into $[Au_2(m\text{-P^P})_2]^{2+}$ (Fig. S38). In contrast, exposure to *o*-P^P ligands triggered a distinct transformation, yielding the cluster $[Au_7(m\text{-P^P})_2(o\text{-}^{nido}P\text{^}P)_2]$ (where $o\text{-}^{nido}P\text{^}P$ = 7,8-bis(diphenylphosphine)-*nido*-carborane, $\mathbf{Au_7}$). Single crystal XRD analysis indicates that $\mathbf{Au_7}$ belongs to the monoclinic *C*2/*c* space group with a regular A–B–A arrangement at the *bc* plane (Fig. S13). The kernel of $\mathbf{Au_7}$ consists of two tetrahedra sharing one gold atom, and two *m*-P^P ligands feature bridging modes to consolidate the two tetrahedra. The two surplus vertices are further occupied by two $o\text{-}^{nido}P\text{^}P$ ligands with chelating coordination patterns (Fig. 3b). The presence of bridging hydrogen atoms at $o\text{-}^{nido}P\text{^}P$ ligands was corroborated by a characteristic signal at $\delta = -2.2$ ppm in the ^1H NMR spectrum (Fig. S39). Fragments of $[Au_2(m\text{-P^P})(o\text{-}^{nido}P\text{^}P)]^+$ (experimental: 1408.4864; simulated: 1408.4848, Fig. S44) and $[Au_2(m\text{-P^P})_2(o\text{-}^{nido}P\text{^}P)]^+$ (experimental: 1919.7628; simulated:1919.7710) are recorded by ESI-TOF MS. The Au–Au bond distances in $\mathbf{Au_7}$ (ranging from 2.618 to 3.214 Å) are significantly shorter than those observed in $\mathbf{Au_{18}}$ and $\mathbf{Au_8}$ nanoclusters with one valence state, implying the presence of zero valence gold atoms accompanied by stronger aurophilic interactions. This is corroborated by XPS analysis: the Au $4f_{7/2}$ peak at 84.2 eV (Fig. S45) lies at an intermediate binding energy between Au(0) and Au(I) species. The divergent reactivity of two diphosphine ligands with similar P···P distances likely originates from the unique structural adaptability of the carborane backbone transforming into a *nido*-carborane structure and the potential reducibility for reduced Au(I) to Au(0).[40]

The UV-Vis absorption spectra of $\mathbf{Au_{18}}$, $\mathbf{Au_8}$ and $\mathbf{Au_7}$ are measured at room temperature in dichloromethane solution. As shown in Fig. 4a, both $\mathbf{Au_{18}}$ and $\mathbf{Au_8}$ display two distinct low-energy absorption bands in the range of 270–280 nm. In contrast, the absorption profile of $\mathbf{Au_7}$ is broadened, spanning approximately 290–310 nm. The optical band gaps of $\mathbf{Au_{18}}$ and

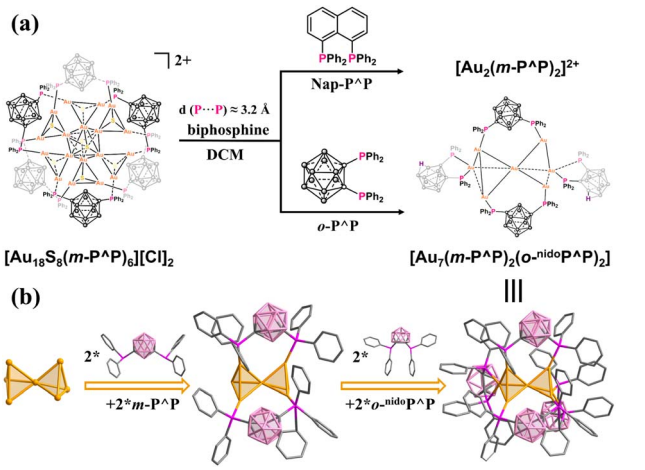

Fig. 3 (a) Structural transformation routes of Au_{18} reacting with bisphosphine ligands with similar P···P distances; (b) single crystal structure of Au_7.

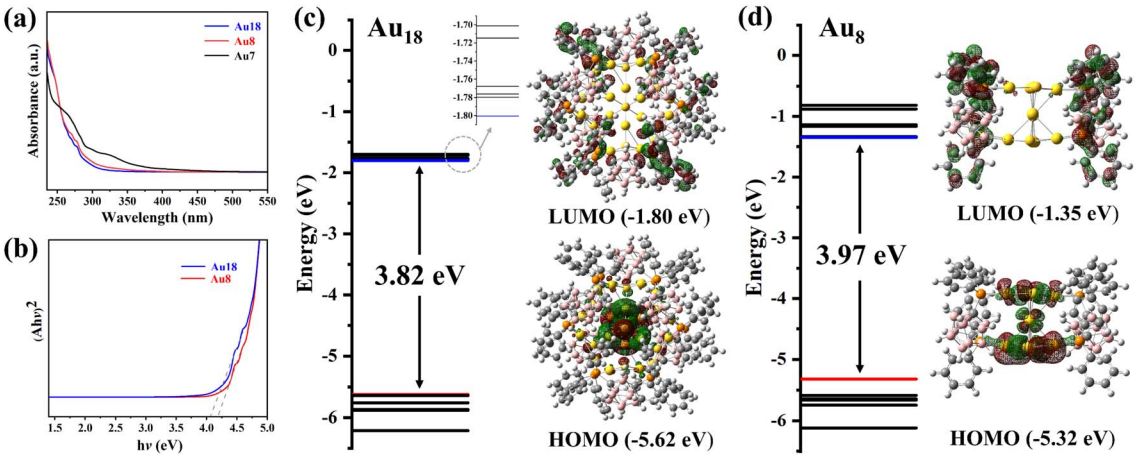

Fig. 4 (a) UV-Vis spectra of Au_{18}, Au_8 and Au_7 in dichloromethane at room temperature; (b) optical band gap of Au_{18} and Au_8. HOMO, LUMO and the calculated energy alignments of (c) Au_{18} and (d) Au_8.

Au_8, calculated using the Kubelka–Munk function are 4.04 eV and 4.18 eV, respectively (Fig. 4b), which are far higher than those of typical semiconductors.

These gold clusters (**Au_{18}**, **Au_8** and **Au_7**) all exhibit orange-red luminescence in the solid state at room temperature, as evidenced by solid-state emission spectra (Fig. S46). Structurally, the transformation from **Au_{18}** to **Au_8** contributes to a red-shift of the emission from 654 nm to 680 nm, while conversion to **Au_7** further shifts it to 776 nm. All of them are non-emissive in solution such as DCM, EtOH, MeOH, acetonitrile, *N*,*N*-dimethylacetamide and *N*,*N*-dimethylformamide. The quenching may be ascribed to the open structural motif, which facilitates non-radiative decay through enhanced solvent and molecular motions.[32]

Carboranes and their derivatives contain a large amount of high-energy density B–B and B–H bonds, endowing them with potential as energetic materials.[47] However, owing to the high stability of carboranes, the exploration of their energy release is still in its infancy. The introduction of "active sites", such as metal salts, has been demonstrated to be an effective strategy for promoting energy release. Herein, 98% white fuming nitric acid (WFNA) was selected to serve as an oxidant to conduct the "oxidizer-to-fuel" droplet test, and the ignition delay time (ID) was recorded using a high-speed camera (2000 dps) to estimate ignition performance (for details see the SI). As shown in Fig. 5a–c, **Au_7** exhibits an ultrafast ID time of 16(2) ms (for more hypergolicity drop tests see Fig. S49 and S50), nevertheless, **Au_{18}** and **Au_8** were not able to be ignited by WFNA in three measurements. Theoretical calculations were performed at the PBE1PBE/def2-SVP level to analyze the molecular orbitals of the nanoclusters. As shown in Fig. 4c and d, the HOMO–LUMO energy gaps of **Au_{18}** and **Au_8** are 3.82 eV and 3.97 eV, respectively. Though the PBE1PBE functional may underestimate the HOMO–LUMO gap,[48] the calculated results are still valuable, and the trend is consistent with their optical band gaps. It is worth noting that **Au_{18}** and **Au_8** exhibit similar electronic distributions in their frontier orbitals: the HOMOs of both clusters are primarily localized on the gold(I)–chalcogenide kernel, whereas the LUMOs are dominated by the surrounding *m*-P^P ligands. Therefore, when **Au_{18}** and **Au_8** react with WFNA, a substantial energy gap between the gold(I)–chalcogenide kernel and *m*-P^P ligands must be overcome.

As a matter of fact, solely the bisphosphine *m*-P^P ligand can be ignited by WNFA with an ID time of 1308 ms (Fig. S51) but cannot be ignited by the introduction of gold(I)–chalcogenide kernels.

We infer that the Lewis-basic S^{2-} in the $[Au_3S]^+$ structural motif hinders WFNA from reacting with high-energy *m*-P^P ligands and also impedes the potential catalytic effects of gold(I). Through ligand-exchange strategies, a no-sulfur **Au_7** nanocluster was obtained with stable ultrafast ID times of 14, 15, and 18 ms for three measurements, and the highest flame temperature reached up to 669.12 °C (Fig. 5d and S48). The calculated band gaps for the α- and β-electronic energy gaps of **Au_7** are 1.01 eV and 3.43 eV, respectively (Fig. S47). The contributions of HOMO and LUMO (both α- and β-electronic) are mainly concentrated on gold kernels, indicating that metal kernels make great contributions throughout the ignition process. The *o*-P^P ligand exhibits a faster ID time of 114 ms compared with the *m*-P^P ligand (Fig. S52). Furthermore, the deboration of the *o*-P^P ligand (*o*-^{nido}P^P) with open architecture may also provide potential reaction sites to accelerate the ID time.

To further evaluate **Au_7** as a potential hypergolic material, the thermal behavior of crystal **Au_7** was investigated by TG-DSC (Fig. 5e). **Au_7** exhibited a gradual mass loss upon heating, attributable to the release of free solvent molecules. The DSC curve recorded a large exothermic peak in the range of 400–650 °C, indicating intense energy release. The heat of combustion (ΔH_c) value of **Au_7**, as measured by oxygen bomb calorimetry (see the SI for details), was determined to be 25.3 kJ g^{-1}. Additionally, its impact sensitivity (IS) and friction sensitivity (FS) were determined using the BAM standard (see Table S5 for the summary of physicochemical properties). The measured values (IS > 40 J and FS > 360 N) indicated that **Au_7** can be classified as an insensitive energetic material.

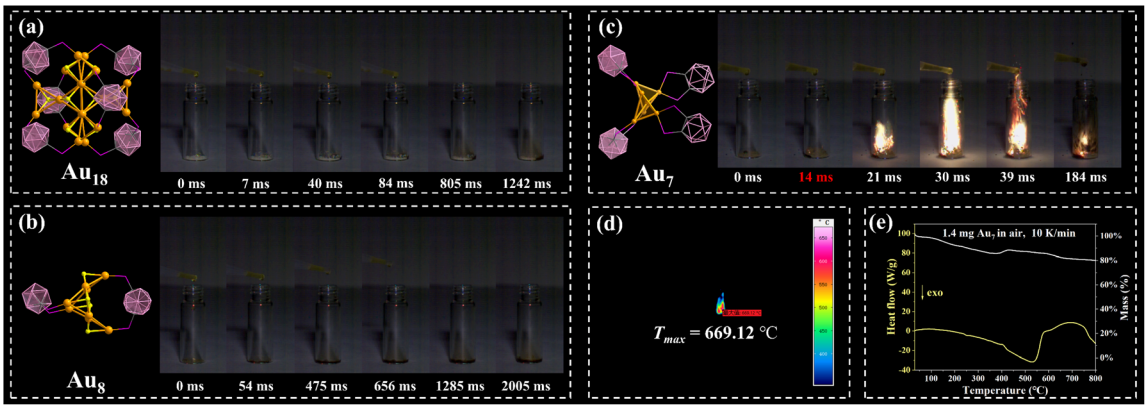

Fig. 5 Hypergolicity drop test of (a) Au_{18}, (b) Au_8 and (c) Au_7. Full videos of Au_7 are provided in the SI; (d) highest flame temperature of Au_7; (e) TG-DSC of Au_7.

Conclusions

Guided by gold(I) aurophilic interactions and bulky carborane ligands, a novel class of structurally induced gold(I)–chalcogenide clusters has been assembled. Our findings demonstrate that the selection of three-dimensional bulky ligands could effectively suppress the aggregation of high-nuclearity metal kernels, and the carborane backbone exhibits unique adaptability through its abilities to undergo deboronation and reduction under mild conditions. The removal of sulfur atoms from gold nanoclusters leads to a remarkable enhancement in their hypergolic properties. This work not only establishes a new paradigm for cluster transformation driven by ionic and ligand effects, but also significantly expands the synthetic toolkit for constructing clusters with tunable functionalities.

Author contributions

Hao-Hui Xie: conceptualization, validation, investigation, formal analysis, writing – original draft, visualization. Wen-Jing Yang & Ze-Jian Li: validation, investigation, resources. Ying-Zheng Ren, Nian Si & Peng-Fei Liu: formal analysis, investigation. Yong-Xing Tang, Wen-Chao Zhang & Peng-Fei Cui: supervision, project administration, funding acquisition.

Data availability

CCDC 2454644–2454647, 2495510–2495512, 2495585 and 2504018 contain the supplementary crystallographic data for this paper.[49a–i]

Supplementary information: experimental details, single-crystal structure X-ray diffraction data, NMR data, and other data. See DOI: https://doi.org/10.1039/d6sc01070a.

Conflicts of interest

There are no conflicts to declare.

Acknowledgements

This work was supported by the National Natural Science Foundation of China (22031003), Open Funding Project of Key Laboratory of Functional Molecular Solids, Ministry of Education, Nankai University (FMS2025003), and Special Fund for Basic Scientific Research Business Expenses of Central Universities (2025201012). We thank the Instrumental Analysis and Testing Center of Nanjing University of Science and Technology for assistance with measurements.

References

1 Z. X. Li and C. Tang, Structure, synthesis and catalysis of ligated Au_3 and Au_4 species, *Coord. Chem. Rev.*, 2026, **549**, 217278, DOI: 10.1016/j.ccr.2025.217278.
2 S. Biswas, A. K. Das and S. Mandal, Surface Engineering of Atomically Precise M(I) Nanoclusters: From Structural Control to Room Temperature Photoluminescence Enhancement, *Acc. Chem. Res.*, 2023, **56**(13), 1838–1849, DOI: 10.1021/acs.accounts.3c00176.
3 A. Ghosh, A. Sagadevan, K. Murugesan, S. A. F. Nastase, B. Maity, M. Bodiuzzaman, A. Shkurenko, M. N. Hedhili, J. Yin, O. F. Mohammed, M. Eddaoudi, L. Cavallo, M. Rueping and O. M. Bakr, Multiple neighboring active sites of an atomically precise copper nanocluster catalyst for efficient bond-forming reactions, *Mater. Horiz.*, 2024, **11**(10), 2494–2505, DOI: 10.1039/d4mh00098f.
4 M. M. Gan, J. Q. Liu, L. Zhang, Y. Y. Wang, F. E. Hahn and Y. F. Han, Preparation and Post-Assembly Modification of Metallosupramolecular Assemblies from Poly(*N*-Heterocyclic Carbene) Ligands, *Chem. Rev.*, 2018, **118**(19), 9587–9641, DOI: 10.1021/acs.chemrev.8b00119.
5 L. M. Zheng, Z. C. Long, F. Hu, J. Chan, W. Q. Shi, B. Zhang, Z. Wang and Q. M. Wang, Solvent Induced Transformation of Homoleptic Alkynyl-Protected Large Silver Nanoclusters, *Angew. Chem., Int. Ed.*, 2025, **64**(26), e202506971, DOI: 10.1002/anie.202506971.
6 Z. C. Yang, Z. Y. Chen, B. Li, R. X. Zhang, Y. T. Cao, D. E. Jiang, Q. F. Yao, H. T. Shan, T. K. Chen, P. Zhang and

J. P. Xie, Integrating Sulfido Ligands into Thiolate-Gold(I) Clusters via Competing Bonding, *CCS Chem.*, 2025, **7**(4), 1100–1111, DOI: 10.31635/ccschem.024.202404942.

7 W. W. Xu, X. C. Zeng and Y. Gao, $Au_3(\mu_3\text{-}S)(0e)$ elementary block: new insights into ligated gold clusters with μ_3-sulfido motifs, *Nanoscale*, 2017, **9**(26), 8990–8996, DOI: 10.1039/c7nr03508j.

8 D. M. Mingos, Structural and bonding patterns in gold clusters, *Dalton Trans.*, 2015, **44**(15), 6680–6695, DOI: 10.1039/c5dt00253b.

9 Q. Liu, X. Y. Zhai, R. J. Jian and L. Zhao, Divergent catalytic behaviors of assembled organogold(I) clusters derived from enyne cyclization, *Chem. Sci.*, 2024, **15**(29), 11311–11320, DOI: 10.1039/d4sc01618a.

10 J. Sun, W. Cheng, X. Liu, H. Xiang, C. Ruan, F. Chen and C. Yao, Gold clusters: a promising NIR-II probe for bioimaging and biosensing, *Coord. Chem. Rev.*, 2025, **533**, 216544, DOI: 10.1016/j.ccr.2025.216544.

11 X. Y. Chen, L. Y. Li, L. C. Zhao, Q. Y. Liu, D. D. Ding, L. L. Zhang, X. Y. Sun, L. K. Wang, H. B. Mo, J. Yan and C. Liu, Ag^+-Mediated Structural Reconstruction of a Metastable Cu_{35} Cluster toward Cu-Ag Heterometallic Architectures for Superior Electrocatalytic CO_2-to-Ethanol Conversion, *Angew. Chem., Int. Ed.*, 2025, **64**(36), e202511232, DOI: 10.1002/anie.202511232.

12 J. R. Shakirova, E. V. Grachova, V. V. Gurzhiy, S. K. Thangaraj, J. Janis, A. S. Melnikov, A. J. Karttunen, S. P. Tunik and I. O. Koshevoy, Heterometallic Cluster-Capped Tetrahedral Assemblies with Postsynthetic Modification of the Metal Cores, *Angew. Chem., Int. Ed.*, 2018, **57**(43), 14154–14158, DOI: 10.1002/anie.201809058.

13 E. S. Smirnova, J. M. Munoz Molina, A. Johnson, N. A. Bandeira, C. Bo and A. M. Echavarren, Polynuclear Gold $[Au^I]_4$, $[Au^I]_8$, and Bimetallic $[Au^I_4Ag^I]$ Complexes: C–H Functionalization of Carbonyl Compounds and Homogeneous Carbonylation of Amines, *Angew. Chem., Int. Ed.*, 2016, **55**(26), 7487–7491, DOI: 10.1002/anie.201603200.

14 M. C. Gimeno and A. Laguna, Chalcogenide centred gold complexes, *Chem. Soc. Rev.*, 2008, **37**(9), 1952–1966, DOI: 10.1039/b708618k.

15 A. Jana, V. Yadav, M. Kucerakova, S. Malola, A. R. Kini, S. Acharya, A. K. Poonia, J. Machacek, K. Adarsh, H. Hakkinen, *et al.*, $[Ag_{62}S_{12}(CBT)_{32}]^{4+}$: A 2.2 nm Two-Electron Superatomic Carborane-Thiolated Silver Nanocluster Exhibiting Multilayer Charge Separation, *ACS Nano*, 2025, **19**(39), 35015–35026, DOI: 10.1021/acsnano.5c11836.

16 M. S. Q. Zhu, Y. D. Yao, Z. H. Liu, D. Chen, J. Yang, Q. F. Yao, W. P. Hu, Z. Y. Jiang and J. P. Xie, Ligand Body Reorganization of Metal Nanoclusters for Enhanced Electrocatalytic CO_2 Reduction Reactivity, *Angew. Chem. Novit*, 2025, **1**(1), e70001, DOI: 10.1002/anov.70001.

17 R. P. Herrera and M. C. Gimeno, Main Avenues in Gold Coordination Chemistry, *Chem. Rev.*, 2021, **121**(14), 8311–8363, DOI: 10.1021/acs.chemrev.0c00930.

18 J. M. Stauber, E. A. Qian, Y. Han, A. L. Rheingold, P. Kral, D. Fujita and A. M. Spokoyny, An Organometallic Strategy for Assembling Atomically Precise Hybrid Nanomaterials, *J. Am. Chem. Soc.*, 2020, **142**(1), 327–334, DOI: 10.1021/jacs.9b10770.

19 C. L. Lin, X. Lei, Y. Zhang, H. Wang, H. Li, Y. Zhao, S. Zhang, W. Fan, W. W. Xu and M. B. Li, Controlling Chirality and Stability of Gold Nanoclusters by PNP Pincer Ligand Diastereomers, *Nano Lett.*, 2025, **25**(29), 11374–11381, DOI: 10.1021/acs.nanolett.5c02514.

20 C. Zhu, B. Li, C. Li, L. Y. Lu, H. Li, X. H. Yuan, X. Kang, D. E. Jiang and M. Z. Zhu, Arylation of gold nanoclusters and insights into structure-related CO_2 reduction reaction performances, *Chem. Sci.*, 2025, **16**(23), 10273–10281, DOI: 10.1039/d5sc01200g.

21 J. Q. Wang, R. L. He, W. D. Liu, Q. Y. Feng, Y. E. Zhang, C. Y. Liu, J. X. Ge and Q. M. Wang, Integration of Metal Catalysis and Organocatalysis in a Metal Nanocluster with Anchored Proline, *J. Am. Chem. Soc.*, 2023, **145**(22), 12255–12263, DOI: 10.1021/jacs.3c02567.

22 Q. Yao, V. Fung, C. Sun, S. Huang, T. Chen, D. E. Jiang, J. Y. Lee and J. P. Xie, Revealing isoelectronic size conversion dynamics of metal nanoclusters by a noncrystallization approach, *Nat. Commun.*, 2018, **9**(1), 1979, DOI: 10.1038/s41467-018-04410-6.

23 L. Y. Yao, F. K. Hau and V. W. Yam, Addition reaction-induced cluster-to-cluster transformation: controlled self-assembly of luminescent polynuclear gold(I) μ_3-sulfido clusters, *J. Am. Chem. Soc.*, 2014, **136**(30), 10801–10806, DOI: 10.1021/ja505599v.

24 Q. Yao, X. Yuan, V. Fung, Y. Yu, D. T. Leong, D. E. Jiang and J. Xie, Understanding seed-mediated growth of gold nanoclusters at molecular level, *Nat. Commun.*, 2017, **8**(1), 927, DOI: 10.1038/s41467-017-00970-1.

25 Z. Lei, X. K. Wan, S. F. Yuan, Z. J. Guan and Q. M. Wang, Alkynyl Approach toward the Protection of Metal Nanoclusters, *Acc. Chem. Res.*, 2018, **51**(10), 2465–2474, DOI: 10.1021/acs.accounts.8b00359.

26 X. Z. Li, S. Mitchell, Y. Y. Fang, J. Li, P. R. Javier and J. Lu, Advances in heterogeneous single-cluster catalysis, *Nat. Rev. Chem.*, 2023, **7**(11), 754–767, DOI: 10.1038/s41570-023-00540-8.

27 R. K. Gupta, Z. Wang, B. Mohan, C. H. Tung and D. Sun, Atomically Precise Coinage Metal Nanoclusters with Exposed Metal Sites: Unlocking Reactivity and Functionality, *Adv. Funct. Mater.*, 2025, 2507047, DOI: 10.1002/adfm.202507047.

28 L. Wang, J. R. Du, J. H. Wu, Z. A. Nan, S. M. Li, X. K. Tang, Z. L. Xie, Q. H. Xu, X. K. Gong, J. L. He, R. H. Chen, N. F. Zheng and H. Shen, Triphenylamine-Functionalized Metal Nanoclusters for Efficient and Stable Perovskite Solar Cells, *Adv. Sci.*, 2025, **12**(1), e2410796, DOI: 10.1002/advs.202410796.

29 Z. Gan, N. Xia and Z. Wu, Discovery, Mechanism, and Application of Antigalvanic Reaction, *Acc. Chem. Res.*, 2018, **51**(11), 2774–2783, DOI: 10.1021/acs.accounts.8b00374.

30 L. L. Ma, Y. Li, X. Li, L. Zhang, L. Y. Sun and Y. F. Han, A Molecular "A-Type" Tangled Metallocube, *Angew. Chem.,*

Int. Ed., 2022, **61**(35), e202208376, DOI: 10.1002/anie.202208376.

31 C. Y. Liu, X. R. Wei, Y. Chen, H. F. Wang, J. F. Ge, Y. J. Xu, Z. G. Ren, P. Braunstein and J. P. Lang, Tetradecanuclear and Octadecanuclear Gold(I) Sulfido Clusters: Synthesis, Structures, and Luminescent Selective Tracking of Lysosomes in Living Cells, *Inorg. Chem.*, 2019, **58**(6), 3690–3697, DOI: 10.1021/acs.inorgchem.8b03298.

32 L. L. Yan, L. Y. Yao, M. Y. Leung and V. W.-W. Yam, Substituent-Mediated Transformation of Polynuclear Gold(I)-Sulfido Complexes—From Pentanuclear to Octadecanuclear Cluster-to-Cluster Transformation, *CCS Chem.*, 2021, **3**(8), 326–337, DOI: 10.31635/ccschem.021.202000662.

33 L. Y. Yao, K. H. Low and V. W. W. Yam, A Gold Quartet Framework with Reversible Anisotropic Structural Transformation Accompanied by Luminescence Response, *Chem*, 2019, **5**(9), 2418–2428, DOI: 10.1016/j.chempr.2019.06.012.

34 L. L. Yan and V. W. Yam, Evolution of Polynuclear Gold(I) Sulfido Complexes from Clusters and Cages to Macrocycles, *J. Am. Chem. Soc.*, 2024, **146**(1), 609–616, DOI: 10.1021/jacs.3c10381.

35 S. S. Zhang, L. Feng, R. D. Senanayake, C. M. Aikens, X. P. Wang, Q. Q. Zhao, C. H. Tung and D. Sun, Diphosphine-protected ultrasmall gold nanoclusters: opened icosahedral Au_{13} and heart-shaped Au_8 clusters, *Chem. Sci.*, 2018, **9**(5), 1251–1258, DOI: 10.1039/c7sc03566g.

36 Y. Shichibu and K. Konishi, HCl-induced nuclearity convergence in diphosphine-protected ultrasmall gold clusters: a novel synthetic route to "magic-number" Au_{13} clusters, *Small*, 2010, **6**(11), 1216–1220, DOI: 10.1002/smll.200902398.

37 S. Takano and T. Tsukuda, Amplification of the Optical Activity of Gold Clusters by the Proximity of BINAP, *J. Phys. Chem. Lett.*, 2016, **7**(22), 4509–4513, DOI: 10.1021/acs.jpclett.6b02294.

38 H. H. Xie, L. J. Zhou, P. F. Cui and W. C. Zhang, Icosahedral carboranes-based metal nanoclusters: from fascinating structures to polychrome properties and applications, *Coord. Chem. Rev.*, 2025, **542**, 216803, DOI: 10.1016/j.ccr.2025.216803.

39 A. R. Kini, S. Debta, A. Jana, C. Aparna, V. Yadav, N. Kusiak, T. Base, U. V. Waghmare, P. Ghosh and T. Pradeep, Nanomechanical Investigations of Crystals of Copper Nanocluster Isomorphs: Enhanced Hardness of the Low-Density Analogue, *Chem. Mater.*, 2025, **37**(3), 1284–1296, DOI: 10.1021/acs.chemmater.4c03265.

40 J. H. Huang, Y. Cui, Z. Y. Wang and S. Q. Zang, Carborane Meets Metal Nanocluster: New Opportunities in Nanomaterials, *Acc. Chem. Res.*, 2025, **58**(8), 1249–1261, DOI: 10.1021/acs.accounts.5c00033.

41 P. Rojo, A. Riera and X. Verdaguer, Bulky P-stereogenic ligands. A success story in asymmetric catalysis, *Coord. Chem. Rev.*, 2023, **489**, 215192, DOI: 10.1016/j.ccr.2023.215192.

42 L. F. Nan, P. He, T. W. Zhang, Y. R. Dong, C. Feng, T. He, P. F. Li, Y. F. Zhang, Y. Nie and J. Jiao, Chirality-Contiguous Bridged Carboranes: Synergistic Scalable Synthesis and Amplification of Circularly Polarized Luminescence, *J. Am. Chem. Soc.*, 2025, **147**(28), 24430–24441, DOI: 10.1021/jacs.5c03381.

43 K. Jaiswal, N. Malik, B. Tumanskii, G. Ménard and R. Dobrovetsky, Carborane Stabilized "19-Electron" Molybdenum Metalloradical, *J. Am. Chem. Soc.*, 2021, **143**(26), 9842–9848, DOI: 10.1021/jacs.1c03568.

44 P. F. Cui, X. R. Liu and G. X. Jin, Supramolecular Architectures Bearing Half-Sandwich Iridium- or Rhodium-Based Carboranes: Design, Synthesis, and Applications, *J. Am. Chem. Soc.*, 2023, **145**(36), 19440–19457, DOI: 10.1021/jacs.3c05563.

45 H. Yang, S. K. Peng, W. Chen, D. Luo, S. B. Xi, S. Lu, Y.-L. Huang, D.-B. Hao, B. C. Cai, H. Wang, M. Xie, M. D. Li, X. P. Li, G. H. Ning and D. Li, Double-Helical Assembly of a Copper-Silver Hydride Cluster Exhibiting Thermally Activated Delayed Fluorescence, *CCS Chem.*, 2025, **7**(7), 2201–2214, DOI: 10.31635/ccschem.024.202404213.

46 Z. Wang, Y. Wang, T. Y. Xu, L. Li, C. M. Aikens, Z. Y. Gao, M. Azam, C. H. Tung and D. Sun, Temperature-Controlled Selective Formation of Silver Nanoclusters and Their Transformation to the Same Product, *Angew. Chem., Int. Ed.*, 2024, **63**(23), e202403464, DOI: 10.1002/anie.202403464.

47 Q. Y. Wang, J. Wang, S. Wang, Z. Y. Wang, M. Cao, C. L. He, J. Q. Yang, S. Q. Zang and C. W. M. Thomas, *o*-Carborane-Based and Atomically Precise Metal Clusters as Hypergolic Materials, *J. Am. Chem. Soc.*, 2020, **142**, 12010–12014, DOI: 10.1021/jacs.0c04638.

48 K. Rahul, K. Rahul and K. M. Dilip, Accurate Prediction of HOMO–LUMO Gap Using DFT Functional and Application to Next-Generation Organic Telluro[n]Helicenes Materials, *J. Comput. Chem.*, 2025, **46**(18), e70175, DOI: 10.1002/jcc.70175.

49 (*a*) CCDC 2454644: Experimental Crystal Structure Determination, 2026, DOI: 10.5517/ccdc.csd.cc2nd82f; (*b*) CCDC 2454645: Experimental Crystal Structure Determination, 2026, DOI: 10.5517/ccdc.csd.cc2nd83g; (*c*) CCDC 2454646: Experimental Crystal Structure Determination, 2026, DOI: 10.5517/ccdc.csd.cc2nd84h; (*d*) CCDC 2454647: Experimental Crystal Structure Determination, 2026, DOI: 10.5517/ccdc.csd.cc2nd85j; (*e*) CCDC 2495510: Experimental Crystal Structure Determination, 2026, DOI: 10.5517/ccdc.csd.cc2prsbl; (*f*) CCDC 2495511: Experimental Crystal Structure Determination, 2026, DOI: 10.5517/ccdc.csd.cc2prscm; (*g*) CCDC 2495512: Experimental Crystal Structure Determination, 2026, DOI: 10.5517/ccdc.csd.cc2prsdn; (*h*) CCDC 2495585: Experimental Crystal Structure Determination, 2026, DOI: 10.5517/ccdc.csd.cc2prvr2; (*i*) CCDC 2504018: Experimental Crystal Structure Determination, 2026, DOI: 10.5517/ccdc.csd.cc2q1ms6.